Quantum ballistic transport in nanowire junctions

K. S. Chan[1,*] and J. H. Wei[1,2]
[1]*Department of Physics and Materials Science, City University of Hong Kong, Hong Kong, China*
[2]*Department of Physics, Shangdong University, Shangdong, China*
(Received 1 August 2006; revised manuscript received 15 January 2007; published 12 March 2007)

The quantum ballistic transport of electrons through nanowire junctions formed by putting one nanowire (with square, rectangular, and circular cross sections) on top of another wire (the two wires are not lying in the same plane) is studied using tight-binding models and the Green's function approach. Different tight-binding models are considered to find the optimum number of tight-binding sites in the transverse plan for approximating the continuum model in a finite range of energy and also to find the minimal site number for qualitative description of the transport characteristics. Resonant dips and peaks found in the interwire and intrawire conductances can be explained by the formation of bound and quasibound states at the cross junction. How the conduction channels of the wires are coupled together in the formation of the bound and quasibound states are analyzed using the projected Green's functions. Quasibound states unbound in both wires give rise to resonant peaks in the interwire conductance as well as resonant dips in the intrawire conductance. Quasibound states unbound in only one wire give rise to only resonant dips in the intrawire conductance without corresponding resonant peaks in the interwire conductance. Some exception in the latter case is discussed. Reduction of interwire coupling strength is shown to suppress the conductance at energy far from the subband edges. In the weak interwire coupling regime, larger conductances are found at energies close to the subband edges. A comparison of the square and rectangular wire junctions studies is made. Increase in the dimension perpendicular to a square wire junction reduces the interwire conductance and enhances the intrawire conductance. On the other hand, degeneracy of subbands due to the higher symmetry of a square cross section enhances the interwire conductance. Comparison of circular wire junctions with square wire junctions show that some conductance features found in square wire junctions disappear in circular wire junctions owing to the weaker interwire coupling in circular wire junctions, which is the result of a smaller contact area between wires. The energies and probability densities of some bound and quasibound states are also determined and analyzed in the present study.

DOI: 10.1103/PhysRevB.75.125310 PACS number(s): 73.23.Ad, 73.40.Gk, 73.63.Bd, 73.63.Nm

I. INTRODUCTION

In the past several decades, we have seen spectacular technological achievements in the miniaturization of electronic devices and the mass production of integrated circuits with sophisticated functions and high efficiency. However, with the device dimension reaching the nanometer scale, the miniaturization trend slows down and alternative approaches to nanosize device fabrication have to be sought in order to revolutionize the microelectronic technology. A promising candidate among these approaches is one that uses self-assembled nanostructures, such as nanotubes[1–3] or nanowires[4,5] as basic building blocks of nanodevices, nanocircuits, and nanosystems. In this "bottom up" approach, nanostructures are assembled into functional components using processing techniques different from conventional microelectronic techniques. For example, nanowires are organized and aligned to form arrays using a solution-based Langmuir-Boldgett method.[6] The stacking of these organized arrays with different orientations produces nanowire networks, which can then be used to construct nano-circuits[7,8] or subsystems[9–11] by making electrical connections between nanowires at appropriate locations. Since self-assembled nanostructures can easily be fabricated in a laboratory in large quantity with relatively inexpensive nonequilibrium growth processes,[12–15] the fabrication cost of the bottom up approach is low in comparison with the conventional approach. For this reason, the bottom up approach has attracted a great deal of research attention recently.

As a building block of nanodevices, semiconductor nanowires are preferable to carbon nanotubes because their electrical properties can be easily controlled by adding impurities during growth.[16] Recently there were some experimental demonstrations of nanowire devices, such as *p*-*n* junctions,[4] lasers,[17] LED's, transistors,[18,19] built from nanowire cross junctions, which are formed by putting one nanowire on top of another wire. If the oxide layer that separates the two wires in the junction is thin enough, electrons can tunnel from one wire into another wire through the oxide layer. With one of the wires being *p*-type and the other wire being *n*-type, the cross junction becomes a *p*-*n* junction, which is the basic building block of devices such as lasers, light emitting diodes and transistors. At the moment, our understanding of electron transport in nanowire cross junctions is quite limited. It is therefore very useful for the design and development of nanodevices to have a detailed study of electron transport in nanowire cross junctions. Although cross junctions have been studied previously,[20–25] nearly all the theoretical works (except Refs. 22 and 25) focus on junctions formed from wires lying in the same plane and the important issue of the effects of the interwire coupling strength has not been properly addressed.

Stimulated by the recent developments in nanowire devices, here we study electron transport through a nanowire cross junction using the lattice tight-binding (TB) model.[26]

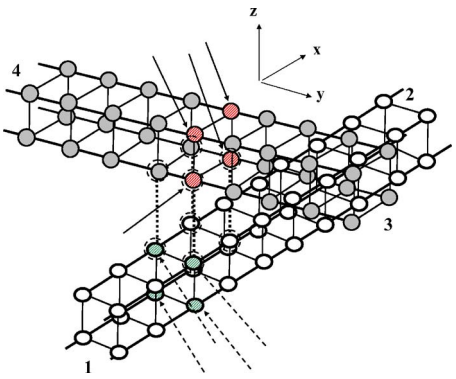

FIG. 1. (Color online) Schematic diagram showing the sites of the tight-binding model of a cross junction formed from two 2×2 square wires. The tight-binding sites connected to sites of the other wire by interwire coupling are circled. The arrows mark the sites considered in the determination of the projected Green's function shown in Figs. 4 and 5. The conducting leads are labeled from 1 to 4.

The main objective of the present work is not to obtain numerical results which can be compared quantitatively with experiments, but to understand the physics of electron transport in a cross junction by identifying generic features in the conductance and investigating how they are affected by the interwire coupling strength. Therefore, lattice tight-binding models with different numbers of conduction channels should be sufficiently accurate for this objective. Some models considered have large numbers of conduction channels and are good approximation of continuum models, which can be used to calculate the nanojunction's conductances in the design of nanowire devices. The organization of this paper is as follows. Section II describes the lattice tight-binding models and the determination of conductance using the Green's function formalism. In Sec. III, the numerical results for different conduction channel numbers and grid sizes are presented and analyzed. The formation of bound and quasibound states are analyzed in terms of the coupling between conduction channels using the projected Green's function. The effects of varying the interwire coupling strength and the cross section are also investigated. The energies and probability densities of some bound and quasibound states are presented and discussed. Finally, the paper is concluded in Sec. IV.

II. MODEL

Figure 1 shows the schematic diagram for one of the lattice TB models considered, in which the TB sites are arranged in a simple cubic lattice structure. At each TB site, there is a single s orbital, which can accommodate one electron without the spin degree of freedom. An electron occupying one TB site can hop to a neighboring site through the hopping terms in the TB model, which are represented by solid black lines connecting neighboring sites of the nanowire in the figure. The nanowire shown in Fig. 1 has a square cross section with four TB sites occupying the square's four corners (it is referred to as a 2×2 square wire) and has four

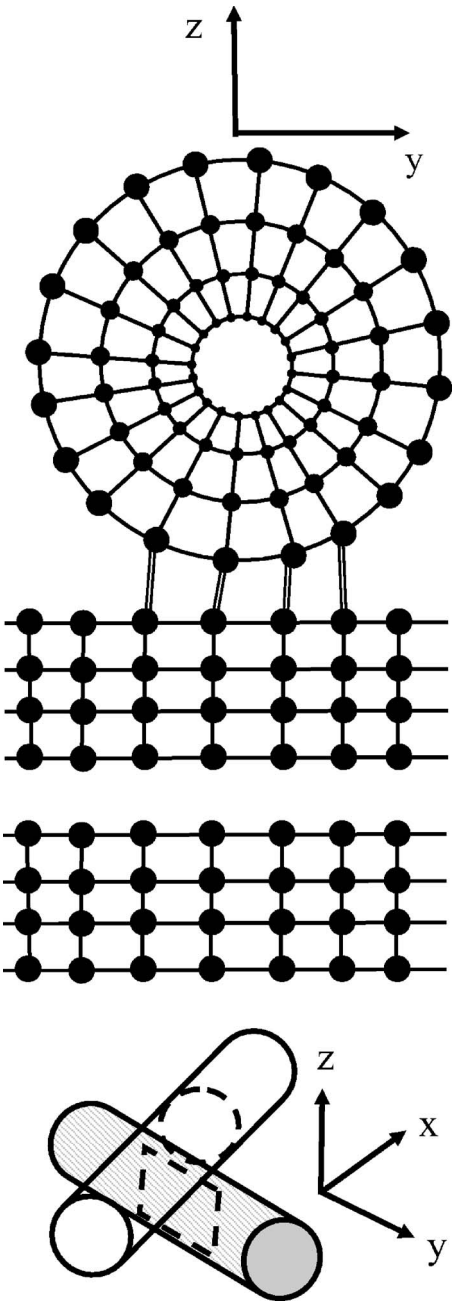

FIG. 2. Schematic diagram showing a cross junction formed from two circular wires. The tight-binding sites in the cross section marked by the dashed circle and rectangle in the junction are also shown.

conduction channels. In addition to this model, we also studied TB models with $N\times N$ square cross section ($N=4,6,8,10$), $N\times N_z$ rectangular cross sections, where N_z denotes the number of sites along the z direction with $N=8$, and $N_z=5,11$. Apart from square and rectangular wires, we also studied cross junctions formed from wires with circular cross section. A schematic diagram of a circular wire junction and the positions of the tight-binding sites in a cross section of the junction is shown in Fig. 2. The position of the cross section is indicated by the dashed circle and rectangle in the figure.

The two wires that form a cross junction are perpendicular to each other and do not lie on the same plane. The transfer of electrons from one wire to another in the cross junction is enabled by the hopping coupling between the TB sites that are in contact (they are nearest neighbors) in the junction. In Fig. 1, these TB sites are circled by dashed circles and the hopping coupling between these TB sites in the cross junctions is represented by dotted lines. The interwire hopping strength is different from the intrawire hopping strength as the hopping probability between two wires is determined by the thickness of the oxide layer between two wires. The interwire hopping strength can be varied between 0 and the intrawire hopping strength in the calculation to investigate the effects of oxide layer thickness on the transport characteristics. When the interwire hopping strength is comparable to the intrawire hopping strength, the junction is in the strong coupling regime and strong mixing of subbands occurs as a consequence. When the interwire hopping strength is much smaller than the intrawire hopping strength or the subband energy separation, the coupling is in the weak coupling regime.

We have considered $N\times N$ square models with large cross-sectional dimensions ($N=6,8,10$) to confirm that TB models can approximate the continuum model. We find that the conductances calculated for $N=8,10$ are quite close in the energy range of interest, which indicates that a TB model with $N=8$ can provide a good approximation to the continuum limit in this energy range. Some TB models with small numbers of conduction channels, 4 channels in a 2×2 square wire and 16 channels in a 4×4 square wire, are also studied in the present study. These two small channel number models were studied for the following reasons:

(1) The simple 2×2 square model, for its relatively small number of channels, can be used to investigate how the conduction channels of different wires are coupled together and the effects of the coupling on the nanojunction's transport characteristics.

(2) By comparing with larger wires, the study of these smaller wires can throw light on the effects of wire diameter on the salient features of the junction conductance.

(3) It is useful to know how good these simple models with small channel numbers can be used to approximate qualitatively TB models with large channel numbers or wires in the continuum limit. These models can be regarded as finite-difference models of large diameter nanowires with coarse discretization grids, which can capture the salient qualitative features of the interaction between conduction channels of different wires. Although these models' accuracy for large diameter wires is not very high, it is still very useful to know for the study of nanowire network structures, which have many nanojunctions formed from a large number of wires, how accurate these simple models can be used to model the transport characteristics of a nanowire junction. One-dimensional (1D) TB model, which has only one TB site in the transverse plane, has been used to model the transmission properties of a two-dimensional (2D) *T*-shaped quantum wire junction by Itoh[27] and qualitative agreement has been obtained between the TB and continuum models for low incident energies. As a result, 1D tight-binding models were adopted to study the physics of other multiterminal quantum wire structures by Xu[28] and Orellana *et al.*[29–31] with significant simplification of the problem. Here we can find the three-dimensional (3D) extension of the 1D model proposed by Itoh.[27]

The tight-binding Hamiltonians for the lower and upper nanowires in the cross junctions are given as

$$H_L = \sum_{i=1,j=-N_L}^{i=M,j=N_L} \varepsilon_L a_{i,j}^+ a_{i,j} + \sum_{i,j} t(a_{R(i),j}^+ a_{i,j} + a_{i,j}^+ a_{i,j+1}) + \text{H.C.},$$

$$H_U = \sum_{i=1,j=-N_L}^{i=M,j=N_L} \varepsilon_U b_{i,j}^+ b_{i,j} + \sum_{i,j} t(b_{R(i),j}^+ b_{i,j} + b_{i,j}^+ b_{i,j+1}) + \text{H.C.},$$

where $a_{i,j}^+(a_{i,j})$ and $b_{i,j}^+(b_{i,j})$ are creation (annihilation) operators of site i,j of the lower and upper nanowires respectively. Index i is the site index along the transverse direction with values between 1 and M, where $M=4$ for a 2×2 square wire and $M=100$ for a 10×10 square wire and, $R(i)$ denotes the transverse index of the nearest neighbor of site i. j is the index along the longitudinal direction with values between $-N_L$ and N_L, and N_L should go to infinity when the wire is infinitely long. $\varepsilon_{L(U)}$ is the orbital energy of the lower (upper) wire and t denotes the intrawire hopping coupling between neighboring sites. For both the square and rectangular wires we use $\varepsilon_L=\varepsilon_U=6t$, which give a bulk energy band bottom at $E=0$. In a $N\times N_z$ rectangular wire with the longitudinal direction along the x axis, there are $N\times N_z$ subbands with dispersions given by

$$E_{ij}(k_x) = 6t - 2t\cos[i\pi/(N+1)] - 2t\cos[j\pi/(N_z+1)] - 2t\cos(k_x),$$

where $i=1,2,\ldots,N$, $j=1,2,\ldots,N_z$, and $-\pi\leqslant k_x\leqslant\pi$. The dispersion for a $N\times N$ square wire can be obtained by putting $N=N_z$.

The total Hamiltonian of the cross-junction is $H_L+H_U+H_T$, where the hopping coupling between the two wires is described by the following term

$$H_T = t_C \sum_{P=1}^{P=K} (a_{\langle P\rangle}^+ b_{\langle P\rangle} + b_{\langle P\rangle}^+ a_{\langle P\rangle}),$$

where t_C is the interwire coupling strength between the upper and lower wires, which is related to the oxide layer thickness between the two wires and can be varied to investigate the effects of oxide layer thickness.$\langle P\rangle$ denotes the indices of sites coupled by H_T and K is the number of sites in each wire participating in the interwire coupling, which equals N^2 for both the square and rectangular wires.

Connected to the cross junction are four semi-infinite conducting leads, which are labeled from 1 to 4 in Fig. 1. To determine the electron transmission probability from one wire to another and the junction's conductance, we consider an incident electron with energy E from lead 1, which is scattered by the cross junction into leads 2, 3, and 4. The transmission probability (conductance) between leads 1 and 2 is the intrawire transmission probability (conductance), while the transmission probabilities (conductance) between lead 1 and leads 3 and 4 are interwire transmission probabili-

ties (conductance). The transmission probability, $T_{pq}(E)$, and conductance $G_{pq}(E)$ between leads p and q at energy E were calculated by using the following expressions[32]

$$G_{pq}(E) = \frac{2e^2}{h} T_{pq}(E)$$

and

$$T_{pq}(E) = \mathrm{Tr}[\Gamma_p(E) G^r(E) \Gamma_q(E) G^a(E)],$$

where $G^r(E)$ and $G^a(E)$ are the retarded and advanced Green's functions of the junction sites at energy E and $\Gamma_p(E) = \Sigma_p^r(E) - \Sigma_p^a(E)$, where $\Sigma_p^{r(a)}(E)$ is the retarded (advanced) self-energy of the junction due to lead p. The retarded and advanced Green's functions are $L \times L$ matrix, where $L = 2N^2 N_z$ is the number of sites in the junction. This expression is only applied to nonidentical leads ($p \neq q$). For the reflection probability ($p = q = 1$), we have to use the following expression

$$T_{11} = N_E - \sum_{p=2}^{4} T_{1p},$$

where N_E is the number of transverse conduction channels participating in conduction at incident energy E. The retarded Green's function can be found as the inverse of the matrix $EI - H_0 - \Sigma_{p=1}^4 \Sigma_p(E)$, where H_0 is the $L \times L$ Hamiltonian matrix of the junction sites without attachment to the four leads, I is an identity matrix and $\Sigma_p(E)$ is the self-energy of lead $p = 1,2,3,4$. To simplify the discussion below, the incident energy and the model parameters are expressed in unit of the intrawire hopping strength, which is assumed to be identical along the longitudinal and transverse directions.

The determination of the transmission probability or conductance of a circular wire junction using the Green's function approach is very similar to a square or rectangular wire junction except for the TB model used to describe the junction and leads. The TB model for a circular wire can be obtained by discretizing the Schrödinger equation as described in Rotter *et al.*[33] The Schrödinger equation is first expressed in cylindrical coordinates z, ρ, and φ, with z denoting the longitudinal coordinate along the length of the wire, and ρ and φ denoting respectively the radial and angular coordinates in the transverse plane of the wire. The discrete grid points for ρ and φ are respectively at $\rho_i = (i - \frac{1}{2})\Delta\rho$, with $i = 1,2,\ldots,N_\rho$ and $\varphi = j\Delta\varphi$, with $j = 1,\ldots,N_\varphi$. N_ρ and N_φ are the numbers of grid points of the two coordinates. The longitudinal coordinate z is discretized with spacing Δz according to $z_k = k\Delta z$, where k is an integer index. In Fig. 2, the TB model has $N_\rho = 4$ and $N_\varphi = 5 \times N_\rho = 20$. Since there are 8 grid points on the diameter of the cross section, the TB model is expected to be a good approximation of the continuum model. This has been confirmed by comparing the results for $N_\rho = 4$ and $N_\rho = 5$.

Applying the variational principle to the discretized Langragian of the system, the TB Hamitlonian $\hat{H}_{cw}^U$ for the upper circular wire (denoted with superscript U) is obtained as

$$\hat{H}_{cw}^U = \sum_k \sum_{i=1}^{N_\rho} \sum_{j=1}^{N_\varphi} (\varepsilon_k^z + \varepsilon_i^\rho + \varepsilon_j^\varphi) a_{i,j,k}^+ a_{i,j,k} + t_{i,i-1}^\rho a_{i,j,k}^+ a_{i-1,j,k} + t_{i,i+1}^\rho a_{i,j,k}^+ a_{i+1,j,k} + t_{j,j-1}^\varphi a_{i,j,k}^+ a_{i,j-1,k} + t_{j,j+1}^\varphi a_{i,j,k}^+ a_{i,j+1,k} + t^z (a_{i,j,k}^+ a_{i,j,k-1} + a_{i,j,k}^+ a_{i,j,k+1}),$$

where $a_{i,j,k}^+ (a_{i,j,k})$ is the creation (annihilation) operator of the TB site i, j, k of the upper circular wire, the TB parameters are given by

$$t^z = \frac{-\lambda}{\Delta z^2}, \quad \varepsilon_k^z = -2t^z,$$

$$t_{i,i\pm1}^\rho = \frac{-\lambda}{\Delta\rho^2} \frac{\rho_{i\pm1/2}}{\sqrt{\rho_{i\pm1}}\sqrt{\rho_i}}, \quad \varepsilon_i^\rho = \frac{2\lambda}{\Delta\rho^2},$$

$$t_{j,j\pm1}^\varphi = -\frac{\lambda}{\rho_i^2 \Delta\varphi^2}, \quad \varepsilon_j^\varphi = \frac{2\lambda}{\rho_i^2 \Delta\varphi^2},$$

$$\text{where } \lambda = \frac{\hbar^2}{2m_e}.$$

For the lower circular wire, the creation (annihilation) operators are represented by $b_{i,j,k}^+ (b_{i,j,k})$. The total Hamiltonian for a circular wire cross junction is $\hat{H}_{cw}^U + \hat{H}_{cw}^L + \hat{H}_C$ where $\hat{H}_C = \Sigma_{I=1}^{N_C} t_C (a_I^+ b_I + b_I^+ a_I)$ is the interwire coupling, with I denoting the indexes of sites that participate in interwire coupling and N_C denoting the total number of these sites. We assume that one fifth of the sites around the circumference participate in interwire coupling and the coupling strength t_C is a constant for these sites. These sites are considered in the interwire coupling because they are the nearest and second nearest neighbors to the sites in the other wire in the junction (farther sites are ignored in this assumption). In reality, the interwire coupling strength depends on the distances between sites and the constant coupling strength used can be regarded as an average effective coupling strength. t_C has been varied in the calculation to examine the effects on conductance. It is found that uncertainties in t_C do not have significant effect on the qualitative features of the conductance; as a result, the constant t_c assumption should not have significant effect on the present study of qualitative features. In the numerical calculation, we assumed $\Delta z = \Delta\rho$ and $\Delta\varphi = \frac{2\pi}{N_\varphi}$, and expressed energy in unit of t^z.

III. RESULTS AND DISCUSSION

A. 2×2 square wire

In this section, the 2×2 square wire model is studied to clarify how the coupling of conduction channels in the junction gives rise to generic features found in the conductance. This simple model is considered first as it can simplify the discussion. The analysis presented in this section provides a basic framework which can be readily used to understand the transport characteristics of junctions formed with wires with larger transverse dimensions.

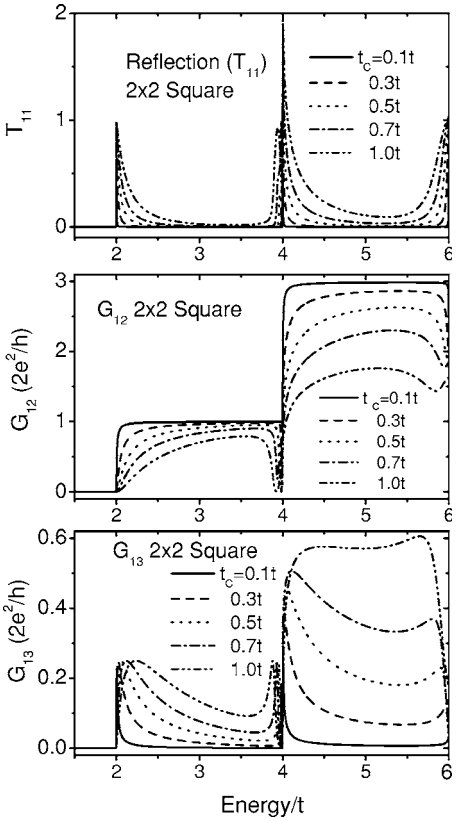

FIG. 3. The reflection T_{11}, intrawire conductance G_{12}, and interwire conductance G_{13} plotted as a function of electron energy for different interwire coupling strengths. The energy unit is the intrawire hopping strength t.

The interwire and intrawire conductances and reflection (respectively, G_{13}, G_{12}, and T_{11}) of the 2×2 square wire are shown in Fig. 3. t_C is varied to investigate the effect of interwire coupling on G_{13} and G_{12}. By symmetry, $G_{13}=G_{14}$ and only G_{13} is shown here. The conductance and reflection of the square wire are symmetrical with respect to $E=6t$ and only results below the symmetry point are shown. In small energy ranges just above the subband edges, strong reflection (T_{11}) can be found, which are associated with the suppression of inter and intra-wire conductances, G_{12} and G_{13}. The sizes of these suppression regions are increased by increasing the interwire coupling strength t_C. This suppression phenomenon is more prominent around the first subband edge than around the second subband edge as the suppression region around the first subband edge is much larger. When t_C is small ($t_C=0.1$), this suppression region in G_{13} is very small and difficult to delineate in the energy scale shown in the figures. Therefore, G_{13} in the weak coupling regime appears to possess sharp peaks at the subband edges. When t_C increases the peak of G_{13} moves away from the subband edges. For energies below the second subband, the peak value of G_{13} equals $0.5e^2/h$, which is independent of the interwire coupling strength, while for energies above the second subband the peak of G_{13} increases with t_C.

Interesting features can also be found in the junction's conductances, G_{12} and G_{13}, at energies around the subband edges. For the 2×2 square wire, two dips in G_{12} and a peak

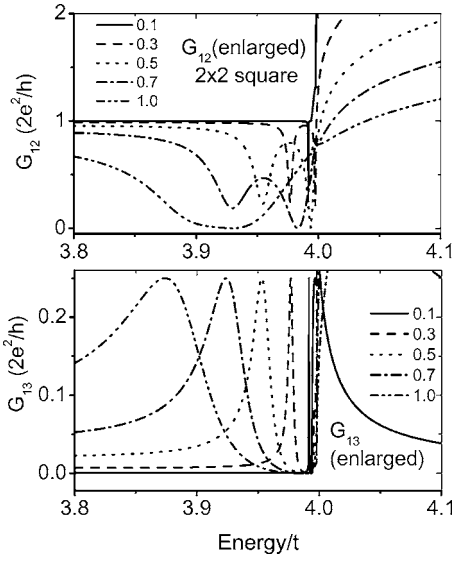

FIG. 4. Enlargement of features of G_{12} and G_{13} in Fig. 3 around the second subband edge ($E=4t$) to show how the dips and peaks are shifted and broadened by increasing t_C.

in G_{13} can be found just below the second subband edge. To further investigate how interwire coupling modifies these features, the conductances are enlarged in Fig. 4, which shows that there are two dips in G_{12} when $t_C=0.3,0.5,0.7$, while when $t_C=1$ there is only one dip in G_{12}. When $t_C=0.1$, the dip in G_{12} is very small. A peak in G_{13} can be found when $t_C=0.3,0.5,0.7,1.0$. The peak height is a constant (equals $0.5e^2/h$). The peaks in G_{13} shifts to lower energies and broadens, when t_C increases.

When two subbands of two identical wires with identical subband energies are coupled together by a strong enough interwire coupling, a bound state can be formed because the mixing of the subbands can lower the electron's energy by allowing the electron to move in a larger space of two wires. If the bound state is formed from second or higher subbands, the bound state can interact with the unbound states of lower subbands and becomes a quasibound state. As a consequence, the only bound state in a junction is formed from the lowest first subbands of the two wires. Higher subbands form quasibound states as a result of the interaction with lower subbands. The quasibound states give rise to features such as dips or peaks in the conductance. To understand the nature of the quasibound states, we analyze some special matrix elements of the Green's function $\langle \eta_U|G|\eta_L\rangle$, where $|\eta_U\rangle$ and $|\eta_L\rangle$ denote states localized respectively in the upper and lower wires. We hereafter referred to this special matrix element as the projected Green's function. In order to find out whether certain higher subbands are mixed together to form the quasibound state, the wave functions $|\eta_U\rangle$ and $|\eta_L\rangle$ should be chosen to have the transverse wave functions of these higher subbands. If these subbands are mixed in the quasibound state, rapidly changing features can be seen in the projected Green's function around the quasibound state energy, if the quasibound state also has a sufficiently long lifetime. The definition and some mathematical properties of the projected Green's function are discussed in detail in Appendix A.

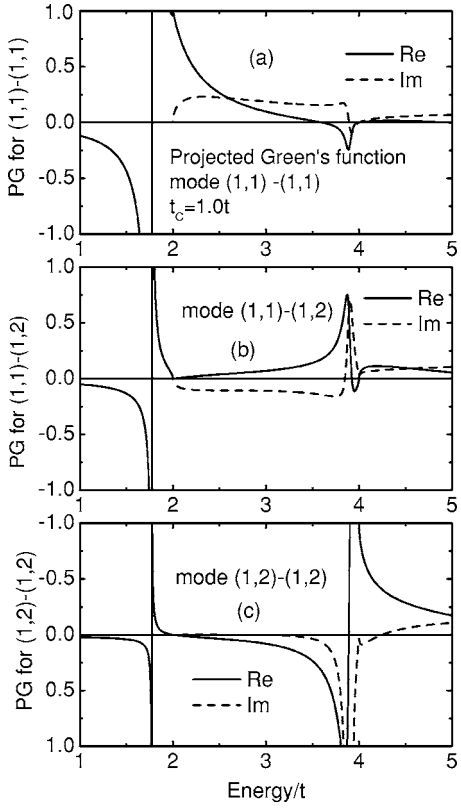

FIG. 5. The projected Green's function calculated with modes (1, 1) and (1, 2) of one wire and modes (1, 1) and (1, 2) of the other wire. Note a bound state and quasibound states are formed below $E=2t$ and $E=4t$. Re represents the real part of the projected Green's function and Im represents the imaginary part. Only $t_C=t$ is considered here.

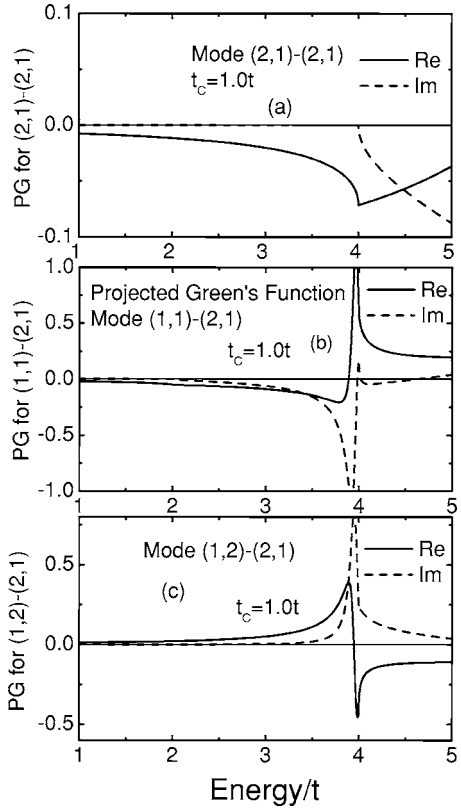

FIG. 6. The projected Green's function calculated with mode (2,1) of one wire and modes (2,1) and (1,1), and (1,2) of the other wire. The condition is the same as Fig. 5.

To understand how the 2×2 square wire's conduction channels are coupled together to form bound and quasibound states, we consider the projected Green's function shown in Figs. 5 and 6, which is obtained using the expression $\langle\psi|G|\phi\rangle=\Sigma_{i,j}\psi(i)G(i,j)\phi(j)$, where $\psi(i)$ is a wave function localized in the upper nanowire and $\phi(j)$ is a wave function localized in the lower nanowire.

To simplify the calculation of the projected Green's function without losing important information, we can choose the wave functions ψ and ϕ to be localized in the TB sites marked by arrows in Fig. 1 (these are sites connected to either lead 1 or lead 3). ψ is a wave function localized in the plane consisting of TB sites marked by solid arrows in the upper wire and ϕ is a wave function localized in the plane consisting of TB sites marked by dashed arrows in the lower wire. In the transverse planes of the wires, ψ and ϕ are eigenfunctions of the transverse modes, which are denoted by (n,m), where n is the transverse mode index along the x (y) direction for the upper (lower) wire and m is the transverse mode index along the z direction. For the 2×2 square wire, there are two transverse modes along each transverse direction $(n,m=1,2)$. Mode 1 is the symmetric transverse mode with a lower eigenenergy, while mode 2 is the antisymmetric transverse mode with a higher eigenenergy. To explain the fine structures in the conductance around the second subband edge at $E=4t$ of a square wire, we only need to consider three of the 4 modes, namely (1,1), (2,1), and (1,2). Mode (1,1) has a subband edge at $E=2t$, while modes (2,1) and (1,2) have their subband edges at $E=4t$.

According to the projected Green's function shown in Fig. 5, channels with the transverse mode (1,1) and mode (1,2) [hereafter the terms, subband (n,m), channel (n,m), and mode (n,m), are used interchangeably to refer to a channel or subband with the transverse mode (n,m)] of the upper and lower wires are coupled together to form a bound state below $E=2t$ and a quasibound state below $E=4t$. Bound states are usually identified as singularities in the real part of the projected Green's function while quasibound states are associated with a peak or some rapidly changing features in the imaginary part of the projected Green's function. If the coupling between channel (1,1) and channel (1,2) of different wires is ignored, the two channel (1,1) from both wires are coupled together to form a bound state below $E=2t$ and the two channel (1,2) from both wires are coupled to form another bound state below $E=4t$. When the coupling between channels (1,1) and (1,2) of different wires are included, the bound state below $E=4t$ becomes quasibound. Incident electron in channel (1,1) in the lower wire can be scattered into the quasibound state and go to channel (1,1) of the upper wire. As a result, the quasibound state below $E=4t$ appears as a transmission resonance between the two wires (as the conductance peak in G_{13} just below $E=4t$ in Fig. 3) and a dip in G_{12}. When t_C increases, the quasibound state energy in-

creases and the resonance peak moves away from $E=4t$ subband edge. The resonance peak also broadens as the quasibound state's lifetime is increased by the interwire coupling t_C. A point worth noting here is that these bound and quasibound states are symmetric with respect to the x and y axes.

Figure 6 shows the projected Green's function calculated by considering channel (2,1) of one wire (for example, the lower wire) and channels (1,1), (1,2), and (2,1) of the other wire (for example, the upper wire). Surprisingly, the coupling of the two channel (2,1) of both wires does not form a bound state [no features are found below $E=4t$ in Fig. 6(a)], because the coupling between these two channels is weak. These two channel (2,1) are antisymmetric with respect to the x or y direction and, as a result, the interwire coupling between these two modes is zero when the longitudinal wave vector $k=0$. Although the interwire coupling does increase with k, the interwire coupling at small k is still too weak to form a bound state. On the other hand, the coupling between the channel (2,1) of the lower wire with channel (1,2) of the upper wire can form a bound state [there is a peak in the projected Green's function in Fig. 6(c)] and this bound state becomes quasibound as channel (2,1) is coupled to the unbound states of channel (1,1) in the upper wire [due to this coupling, features can be found below $E=4t$ in Fig. 6(b)]. This quasibound state can only involve one of the two channel (1,1) of the two wires by symmetry. When the channel (2,1) involved in the quasibound state is in the lower wire, this quasibound state is antisymmetric with respect to the x axis. By symmetry, this quasibound state can only involve channel (1,1) of the upper wire and not the channel (1,1) in the lower wire, which is symmetric with respect to the x axis. This is different from the quasibound state considered in Fig. 5, which is symmetric with respect to both the x and y axes. As a result, this quasibound state is unbound in the upper wire and bound in the lower wire.

By symmetry there is another quasibound state at the same energy which is unbound in the lower wire [involve channel (1,1) of the lower wire] and bound in the upper wire. This quasibound state gives rise to a dip in the intrawire conductance G_{12} without any peak in the interwire conductance G_{13}, because the electron cannot go from lead 1 to lead 3 through this quasibound state. The dip in G_{12} is due to the interference of the two channels of scattering between lead 1 and lead 2. In the presence of the quasibound state (which is unbound in the lower wire and bound in the upper wire), an electron moves from lead 1 to lead 2 can go through two scattering channels: one is through the quasibound state and the other one is directly from lead 1 to lead 2. These two scattering channels interfere leading to a dip in the conductance (transmission). The dip broadens when t_C increases; as a consequence, the two dips in G_{12} merge together to form one dip when $t_C=1$ as shown in Fig. 4.

Similar transmission dips were found in the transmission of an electron in a quantum waveguide coupled to the quasibound states of a resonantor attached to the quantum waveguide and analyzed by Shao *et al.* and Porod *et al.*[34,35] They found exact transmission zeros at the quasibound state energies as the result of the interference of two scattering channels similar to two channels described above. Exact transmission zeros occur in the system studied by Shao *et al.* and Porod *et al.*,[34,35] because the scattering matrix for the two interfering channels is exactly unitary. Here, in a nanowire junction, the current flowing between lead 1 and 2 is not conserved because the electron can be scattered into the upper wire. When an electron goes from lead 1 to lead 2 without going through the quasibound state, the electron has a nonzero probability of scattering into the upper wire by interwire coupling. As a result, the unitary condition is violated and a transmission dip is formed instead of an exact transmission zero in a nanowire junction.

B. Effects of grid size and dimensions

For quantitative comparison with experiments, the lattice TB model should approximate a continuum model, which can be achieved by using a large number of TB sites in the cross section with small grid size. However, to find the Green's function of a lattice TB model with a large number of TB sites is numerically demanding. Therefore, it is very useful for the design of nanowire junction devices, if the optimum number of lattice TB sites can be found for modeling the transport characteristics both quantitatively and qualitatively. To answer this question we compare the results obtained with different grid sizes in Fig. 7, by considering four different $N\times N$ square wire TB models with $N=4,6,8,10$. Since the physical dimensions in the continuum limit are assumed to be identical for these four models, the intrawire hopping strengths and the grid sizes are different for these four models, because the hopping strength is related to the grid size by the relation $t=\hbar^2/8\pi^2ma^2$, where m is the effective mass of the electron in the wire and a is the grid sizes.

Consider the 10×10 TB model with the grid size a and the intrawire hopping strength t_o, the wire in the continuum limit has the transverse physical dimensions $11a\times 11a$. For $N=8,6,4$, the grid sizes are respectively $1.22a$, $1.57a$, and $2.2a$, to have the same continuum transverse dimensions; respectively, the intrawire hopping strengths are $0.67t_0$, $0.406t_0$, and $0.2066t_0$. Here, the energy and other parameters are expressed in unit of t_0, the intrawire hopping strength of the 10×10 square wire. The conductances for these four models are shown in Fig. 7, where one can easily see that the conductances for $N=10$ and $N=8$ models looks similar, which indicates that an $N=8$ model is already accurate enough for approximating the continuum model within the energy range considered. The exact upper limit of the energy range depends on the electron effective mass and grid size. For an electron effective mass of $0.067m_0$, that of GaAs, and a grid size of 9 Å, the upper limit is 0.7 eV, which covers the scope of most studies of low energy characteristics. For smaller $N=4,6$, the qualitative features are very similar to those of $N=8,10$, but the energy positions of the dips and peaks in the conductance are very different quantitatively. The qualitative difference between $N=2$ and $N=10$ results is significant, suggesting that a 4×4 square wire model can be used as the 3D extension of Itoh's model.

These results can also be used to understand the effects of cross-sectional dimensions on the conductance. By rescaling the energy so that the hopping strengths are identical in these

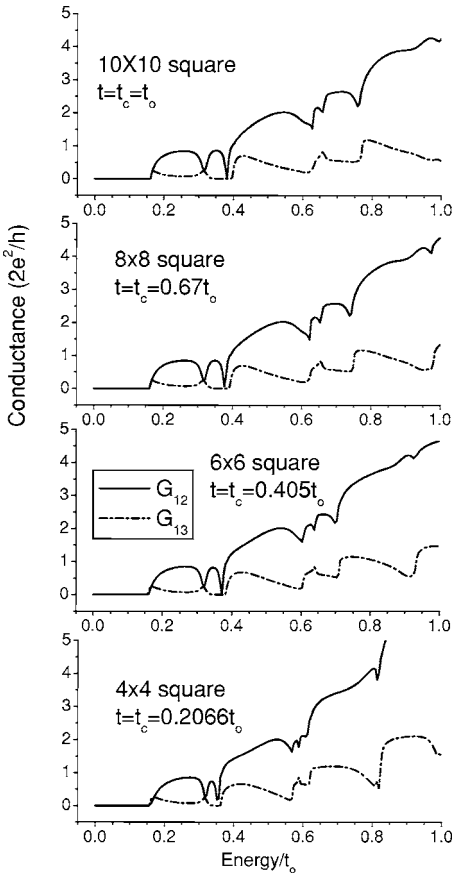

FIG. 7. Intrawire (G_{12}) and interwire (G_{13}) conductances plotted as a function of electron energy. The unit of energy is t_0, the intrawire hopping strength of the 10×10 square model. Only $t=t_C$ is considered. Different wires have different intrawire hopping strength so that the physical dimensions of these models in the continuum limit are identical. Note that the qualitative features of the conductances do not depend on the wire's transverse dimension.

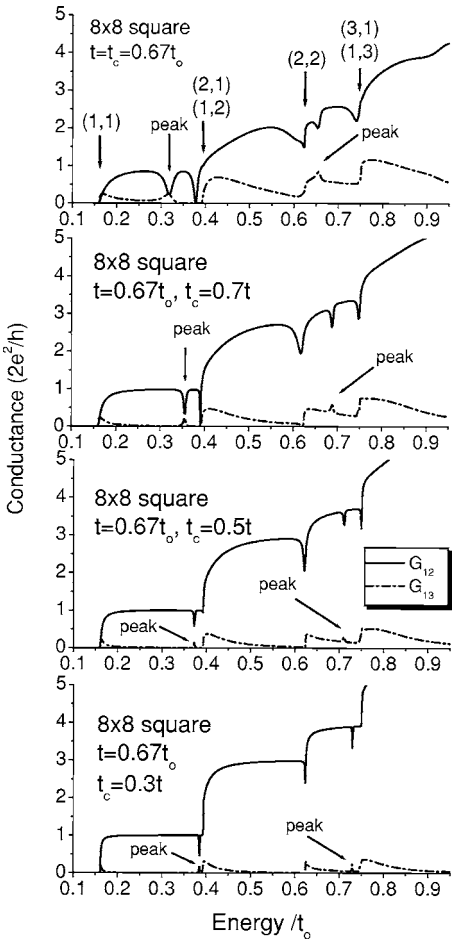

FIG. 8. The inter and intrawire conductances of a 8×8 square model plotted as a function of electron energy (energy unit is t_0) for different interwire coupling strength t_C. Mode indices for the subbands are shown in the top figure and the two resonant peaks in G_{13} are marked with arrows. When t_C is small, larger interwire conductance is found near to the subband edges. The two resonant peaks in G_{13} are barely discernible when $t_C=0.3t$.

models, the results can be used to compare wires with different cross-sectional dimensions. For example, the energy scale of the figure for the 4×4 square wire should be divided by 0.2066 for rescaling so that the intrawire hopping strength is t_0. We notice that all the conductances have similar qualitative features despite their differences in the number of TB sites in the transverse plane (different transverse dimensions). This indicates that the nanowire's transverse dimensions do not have significant effect on the qualitative behavior of the junction's conductance. The graphs shown in Fig. 7 are equivalent to plotting the conductances of these wires obtained with identical intrawire hopping strengths t_0 against scaled energy. The energy is scaled by multiplying the energy by a factor, which equals 0.2066, 0.405, 0.67, and 1 when $N=4,6,8,10$ respectively. We notice in Fig. 7 that the scaled conductances are approximately the same in certain range of energies if the differences in the dip and peak positions are ignored. We therefore compared the conductances of wires with $N=2,3,\ldots,10$ (the intrawire hopping strengths equal t_0) using scaled Fermi energy E_F, which is measured from the first subband edge. The scaling relation used is $E_F(N,\text{Scaled})=E_F(N,\text{Unscaled})\frac{(N+1)^2}{11^2}$. We also found that the conductances for different N are approximately the same as found in Fig. 7, ignoring the differences in the positions of the dips, peaks, and subband edges. The range of agreement depends on the values of N: for $N=2,3,\ldots,10$, the agreement range is between the first subband edge and the second subband edge. For $N=4,5,\ldots,10$, the agreement range is between the first subband edge and third subband edge. For $N=8,9,10$, the agreement range is extended to the fourth subband edge.

C. Effect of interwire coupling strength

Figure 8 shows the conductances of 8×8 square nanowire junctions with different interwire coupling strength t_C, mimicking the effects of different oxide thicknesses between the wires. Note that we use here the intrawire hopping strength $t=0.67t_0$ so that the transverse dimension of the wire is $11a\times11a$ and energy is expressed in unit of t_0. Four subband edges can be identified in the conductance with energies given in Table I. The interwire conductance G_{13} is

TABLE I. Subband energies of nanowire tight-binding models in unit of t_0.

	$E(1,1)$	$E(1,2)$	$E(2,1)$	$E(2,2)$	$E(1,3)$	$E(3,1)$
8×8 *square*	0.161	0.394	0.394	0.627	0.751	0.751
8×5 *rectangle*	0.260	0.751	0.493	0.9835	1.421	0.849
8×11 *rectangle*	0.126	0.260	0.359	0.493	0.473	0.716

decreased by the decrease in t_C, while the intrawire conductance G_{12} is increased. The conductance at energy far from the subband edges decreases much faster than the conductance close to the subband edges. In the weak coupling regime ($t_C=0.3t=0.2t_0$), G_{13} appears to have several asymmetrical peaks, with heights around $0.5\sim 0.7e^2/h$, centering around the subband edges, indicating that only electrons with energy around the subband edges can be effectively transferred to another wire. The widths of these asymmetric peaks depend sensitively on t_C and the subband energy. When the subband energy and t_C are increased, the width is increased. There are two additional peaks, which are more symmetrical in shape, in G_{13} (these two peaks are marked by arrows in the figure and corresponding dips can be found in G_{12} at the same energy) for $t_C=0.3t$ at energies around $0.4t_0$ and $0.7t_0$ (just below the second and fourth subband edges). The positions of these two conductance peaks depends sensitively on t_C and they are at energies $0.3t_0$ and $0.65t_0$ when $t=t_C$ in the strong coupling regime. By measuring the distances of these symmetric conductance peaks from the subband edges in experiments, one can determine the interwire coupling strength of the nanowire junction and hence investigates how the coupling strength is determined by other factors such as the fabrication condition.

These two conductance peaks come from the quasibound states formed, just as discussed in the case of 2×2 square wire, by the mixing of the two channel (1,2) (from different wires) for the first peak and the mixing of two channel (1,3) for the second peak. For the subband edge at energy $0.75t_0$, there are two transverse modes, (1,3) and (3,1). The conductance peak below this subband edge (at $E=0.65t_0$ when $t_C=t$ and it shifts with t_C) comes from the coupling of the two channel (1,3) from different wires, since the coupling between these two modes, which is similar in strength to the coupling of two channel (1,2), should be strong enough to give rise to a discernible quasibound state. The fact that only one peak is found below this subband edge in G_{13} indicates that the coupling between two channel (3,1) is not strong enough to give rise to a discernible quasibound state.

Just as in the 2×2 square wire case, there are dips in the intrawire conductance G_{12} which are not associated with any peaks in G_{13} at energies $0.4t_0$, $0.6t_0$, and $0.75t_0$ (consider the case with $t=t_C$). According to the analysis of the 2×2 square wire case, these quasibound states are bound in one wire and unbound in another wire. The quasibound state at energy $0.4t_0$ comes from the coupling of channel (1,2) of one wire with channel (2,1) of the other wire. Around $E=0.6t_0$, there is a big dip in G_{12}, which seems to be produced by a quasibound state formed from channel (2,2) of one of the wires. Close examination of G_{13} around this energy shows that the channel (2,2) forms two quasibound states very close in energy near to the subband edge at $0.627t_0$, and the two dips in G_{12} due to these quasibound states are not discernible as they merge together. These two dips in G_{12} can be clearly distinguished when they become sharper by reducing the interwire coupling t_C to $0.9t$. By examining the projected Green's function (not shown here for a lack of space), the quasibound state at a higher energy ($E\cong 0.627t_0$) is formed by the mixing of two channel (2,2) of the two wires. In the case of 2×2 square wire, the mixing of two channel (2,1) cannot form any bound state. Here in an 8×8 wire, the mixing of two channel (2,2) can form a discernible quasibound state because of the interaction with the continuum states of channel (2,1). Another quasibound state is formed around $E=0.61t_0$ by mixing channel (2,2) from one wire with channel (1,1) and channel (1,2) from another wire. The latter quasibound state has a very short lifetime and the peak features in the conductance and the projected Green's function are not very prominent. The quasibound state at energy $0.751t_0$ comes from mixing channel (1,3) and channel (3,1) from different wires.

D. Effect of cross section

To investigate the effects of the wire's cross section, we calculated the conductance of two rectangular wires with different N_z ($N=8$ and $N_z=5,11$), and compare with the 8×8 square wire in Fig. 9 (note: different wires use different energy scales). For rectangular wires, increase in the z-direction dimension reduces the interwire conductance G_{13} (increases the intrawire conductance G_{12}), as the wave functions are stretched along the z direction, hence reducing the interwire coupling. Nevertheless, the dependence of G_{13} on the z-direction dimension is not monotonic, as the G_{13} of the 8×8 square wire and the 8×5 rectangular wire are comparable in magnitude, which is due to the higher subband degeneracy found in a square wire. On the other hand, the G_{12} of the 8×5 rectangular wire is significantly smaller than the G_{12} of the 8×8 square wire, implying that the 8×5 rectangular wire has stronger reflection back into lead 1 than the 8×8 square wire. Since the 8×5 wire has a smaller cross-section, the interwire coupling is expected to have stronger scattering effect, which increases the reflection from the junction.

Owing to the removal of subband degeneracy by lowering of symmetry, the dip and peak positions of the rectangular wires are shifted with the subband edges. In Table I, the subband energies for the rectangular wires are shown for easy identification of subbands in Fig. 9. The dips associated with the (2,1) subband are found in the rectangular wires in the new positions ($0.493t_0$, $0.359t_0$). The peak in G_{13} and two dips in G_{12} due to the (1,3) subband moves to energy between $0.42t_0$ and $0.47t_0$ in the 8×11 rectangular wire. The dip in G_{12} at $E=0.47t_0$ comes from the quasibound state formed from subbands (1,3) and (2,1). This quasibound state also forms a very small peak in G_{13} as it is coupled with the unbound states of scattering channels formed from the sub-

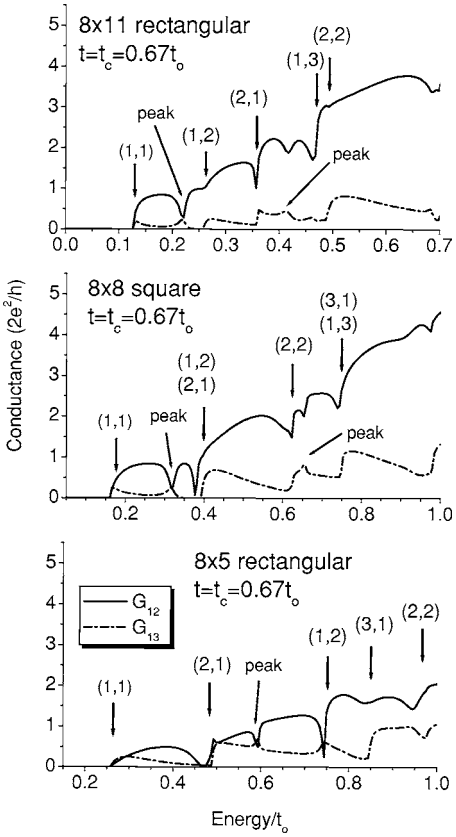

FIG. 9. The inter and intrawire conductances of a 8×5 rectangular wire, a 8×8 square wire and a 8×11 rectangular wire are plotted as a function of electron energy (energy unit is t_0). Mode indices of the subbands are shown and the two resonant peaks in G_{13} are marked by arrows.

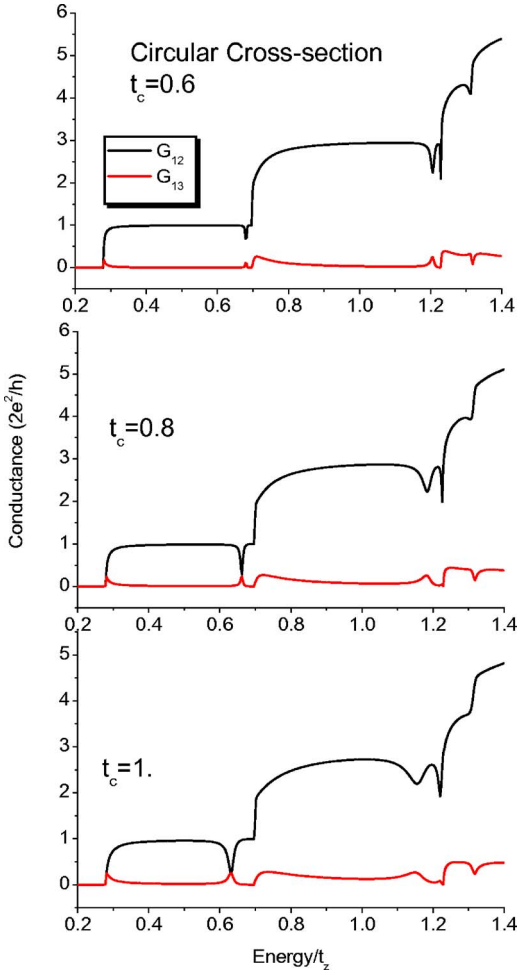

FIG. 10. (Color online) The inter and intrawire conductances of a circular wire junction with $N_\rho=4$ Energy is expressed in unit of t_z.

bands (1,1) or (1,2) of one wire and (2,1) of another wire. In G_{13} of the 8×5 rectangular wire, there is a resonant peak at energy $0.6t_0$, which is associated with a dip in G_{12}. This comes from the quasibound state formed from the channels (1,2) with the subband edge at $E=0.75t_0$, where a dip in G_{12} is found. The G_{13} around the (1,2) subband edge has the shape of an asymmetric peak, showing that a second quasibound state is formed very close in energy to the (1,2) subbands.

E. Conductance of circular wire junctions

Figure 10 shows the conductances of a circular nanowire junction with $t_c=0.6$, 0.8, and 1 (in unit of t_z). The G_{13} of a circular wire junction is in general smaller than that of a square wire junction and smaller suppression of G_{12} is found around the subband edges in a circular wire junction. It is because the contact area between the two circular wires is smaller than that between two square wires and so, for the same t_c and similar transverse dimensions, the effective coupling between two circular wires is smaller than that between two square wires. As a consequence, the maxima of G_{13} in circular wire junctions are closer to the subband edges. Peaks and dips are also found in the conductances of circular wire junctions. The understanding of these features and their comparison with square wires cannot be carried out without the knowledge of the transverse modes of circular wires; therefore, we should first discuss the lowest six transverse mode wave function of a circular wire.

The transverse mode wave function of a circular wire can be separated into an angular part and a radial part, because the continuum Schrödinger equation of a circular wire is separable with respect to the cylindrical coordinates. As a result the eigenfunctions of the TB Hamiltonian of a circular wire can be separated into a longitudinal part F_i, a radial part V_j and an angular part U_k as $\Phi_{i,j,k}=F_iV_jU_k$. The angular part wave function U_j satisfies the eigenvalue equation $\omega V_j=(\lambda/\Delta\varphi^2)[V_{j-1}-2V_j+V_{j+1}]$. ω is the separation constant used to separate the radial part and angular part of the equation and is related to the squared angular momentum. F_i and U_k satisfy respectively the following eigenvalue equations:

$$E(\omega)F_{[\omega],i}=-\frac{\omega}{\rho_i^2}F_{[\omega],i}+\frac{\lambda}{\Delta\rho^2}\left(-\frac{\rho_{i-1/2}}{\sqrt{\rho_{i-1}}\sqrt{\rho_i}}F_{[\omega],i-1}+2F_{[\omega],i}-\frac{\rho_{i+1/2}}{\sqrt{\rho_i}\sqrt{\rho_{i+1}}}F_{[\omega],i+1}\right),$$

TABLE II. Subband energies, mode indices and mode labels of the transverse mode wave functions of the subbands. Energy is expressed in unit of t_z.

Subband	Subband energy (in unit of t_z)	Number of node along radial direction n_ρ	Angular quantum number n	Mode label $[n_\rho, \lvert n\rvert]$
First	0.2777	0	0	[0,0]
Second	0.6985	0	±1	[0,1]
Third	0.6985	0	±1	[0,1]
Fourth	1.2296	0	±2	[0,2]
Fifth	1.2296	0	±2	[0,2]
Sixth	1.3200	1	0	[1,0]

$$EU_k = \frac{-\lambda}{\Delta z^2}(U_{k-1} - 2U_k + U_{k+1}).$$

For a full circle with N_φ TB sites, the angular eigenfunction and eigenvalue for angular quantum number n are

$$V_{[n],i} = \left[\frac{1}{N_\varphi \Delta\varphi}\right]^{1/2} e^{in2\pi j/N_\varphi}, \quad \omega_n = \frac{2\lambda}{\Delta\varphi^2}\left[\cos\left(\frac{2n\pi}{N_\varphi}\right) - 1\right].$$

Here we are only interested in the transfer mode wave function of the lowest six subbands of a wire with $N_\rho = 4$ and $N_\varphi = 20$, the energies and angular quantum number n of which are given in Table II. The first and the sixth subbands both have rotational symmetry ($n=0$) and is symmetric with respect to reflection about the z axis shown in Fig. 2. The second and the third subbands are degenerate and any linear combination of the $n=+1$ and $n=-1$ eigenfunctions is still an eigenfunction of the angular Hamiltonian. The linear combination can be constructed in such a way that the resulting eigenfunction is either symmetric or antisymmetric with respect to reflection about the z axis shown in Fig. 2. The symmetrization and antisymmetrization of eigenfunctions can also be applied to the third and fourth subbands, which are degenerate. In general symmetrized eigenfunctions have larger electron density at the sites involved in interwire coupling, and therefore experience stronger interwire coupling. In an antisymmetrized eigenfunction, there is a node between the middle two coupling sites leading to smaller density at coupling sites and weaker interwire coupling.

For the analysis of the conductance, it is also useful to compare the probability densities of the transverse modes of circular and square wires. For the lack of space, the probability density of the transverse modes of a circular wire is not shown here. The probability density of the symmetrized eigenfunction of $n=\pm 1$ subbands resembles the mode (1,2) of a square wire, while the antisymmetrized eigenfunction resembles the mode (2,1) of a square wire. We therefore expect to find peak and dip structures in the conductance just below the second and third subband edges similar to those found in a square wire junction. However, in the conductance for circular nanowire junction shown in Fig. 10, we find the dip and peak structure for the subband with symmetrical transverse eigenfunction. For the antisymmetrical transverse mode, the dip in G_{12} due to the coupling to a symmetrized mode of the other wire is not present in the circular wire junction. Our explanation is the smaller binding energy and longer lifetime of this quasibound state in a circular wire junction, which has weaker interwire coupling. When this binding energy is very small, the dip in G_{12} is very close to the subband edge; thus, it is not easy to resolve this sharp dip from the subband edge.

For the fourth and fifth degenerate subbands, the subband with symmetrical transverse wave function resembles the mode (1,3) in the square wire junction, because sites participating in interwire coupling lies between two nodes of the angular wave function. Strong interwire coupling is expected for this mode and the dip in G_{12} and the peak in G_{13} below the subband edge are attributed to the quasibound state formed from this subband. For the subband with an antisymmetrical transverse wave function, the mode profile resembles that of (2,2) in the square wire and a dip in G_{12} is found near to the subband edges. For energies below the second and third subbands, the conductances of circular and square wire junctions look very similar, except for the disappearance of a dip in G_{12} in the circular junction. For energies around the fourth and fifth subbands, the qualitative features are very similar in both circular and square wire junctions and have the same physical origin. Nevertheless, the energy locations of these features are different owing to the differences in subband energies between circular and square wires. The sixth subband in the circular junction has a symmetrical transverse mode profile and is expected to give rise to a dip in G_{12} and a peak in G_{13} as for mode (1,2) in square wire junctions. In Fig 10, a dip in G_{12} and a small peak in G_{13} are clearly found just below the sixth subband, when $t_c = 0.6$. However, for $t_c = 1$, these features are not that prominent. The explanation is that when interwire coupling is strong the quasibound state has shorter lifetime and the peak and dip are so broad to be clearly seen in the conductance curve.

F. Bound and quasibound state energies

To find the quasibound state energies, we added all the local density of states (LDOS) in the scattering region and plotted the sum as a function of energy, according to $\rho(E) = \Sigma_I \mathrm{Im}[G_{I,I}(E)]$, where I denotes the sites of the scattering

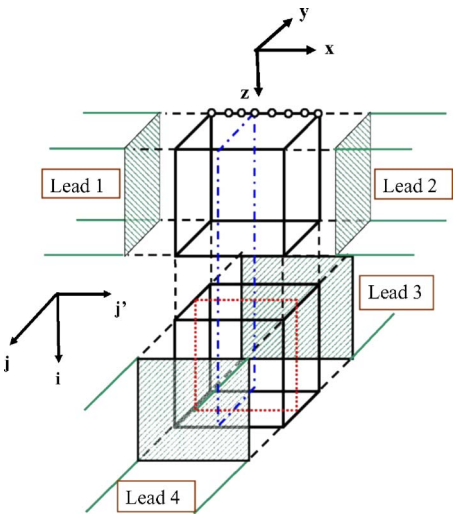

FIG. 11. (Color online) Schematic diagram of a square wire junctions shown the positions of several cross sections which are used in the determination and display of bound and quasibound state probability densities. The blue dot-dashed plane is the 8×16 cross section in which the probability density is shown in Figs. 12 and 13. The red dotted plane is the 8×8 cross section for the probability density shown in Fig. 13

region. In the junction of two 8×8 square wires, the scatter region is an $8\times8\times16$ prism, which is the region bound by the green hatched planes in Fig. 11. Sharp peaks in $\rho(E)$ can be found at the energies of some conductance dips and peaks, indicating that the quasibound states have larger probability density within the scattering region and long lifetimes. In these cases, the quasibound state energy E_B is found from the peak of $\rho(E)$ which can be approximated by $A^2/(E-E_B+i\Gamma)$. To find the energy of the bound state below the first subband (here $\Gamma=0$), we find the position of the singularity in the real part of $\Sigma_I G_{I,I}(E)$. Table III shows the bound and quasibound state energies E_B's for square and circular wire junctions with different transverse dimensions. In both junctions, E_B decreases with increase in the transverse dimension, indicating that stronger quantum confinement in smaller wires leads to formation of stronger bound states at the junction. The quasibound state of $(2,2)\leftrightarrow(2,2)$ in the square wire junction is weakly bound and has very small $E_B\leqslant5\times10^{-4}$. The symbol $\leftrightarrow$ is is used hereafter between two modes to denote that the two modes are coupled to form the bound (or quasibound) states. For the three bound (or quasibound) states of $(1,1)\leftrightarrow(1,1)$, $(1,2)\leftrightarrow(1,2)$, and $(1,3)\leftrightarrow(1,3)$, E_B increases with the number of nodes on the z axis, because the electron density at the interacting sites increases with the number of nodes along the z axis.

In circular wire junctions, the quasibound state of $[1,0]\leftrightarrow[1,0]$ has E_B decreasing with decrease in wire diameter. In this case, the quasibound state energy is very small, and is therefore affected strongly by the coupling to the unbound states of lower subbands. When the wire diameter is increased, the subband separation is reduced and the quasibound state energy is then lowered by a stronger coupling to the lower subbands. It is also noted (by comparing states with $n=0$ and 1) that quasibound states formed from subbands with nonzero angular momentum ($n>0$) have larger E_B than that from subbands with $n=0$. The reason is that subbands with $n>0$ have larger electron probability density at the circumference of the wire and, hence, have stronger interwire coupling.

G. Probability density of bound and quasibound states

It is useful for understanding the nature of the bound and quasibound states to study their probability densities in the scattering region. Here we consider three bound or quasibound states of the 8×8 square wire junction. The two qua-

TABLE III. Bound and quasibound state energies of square and circular wire junctions measured from the corresponding subband edges. For square wire junction, energy is in unit of t_0. For circular wire junction, energy is in unit of t_z.

	E_B (square wire)		
Modes coupled	7×7 square wire	8×8 square wire	9×9 square wire
$(1,1)\leftrightarrow(1,1)$	0.0471	0.0389	0.0317
$(1,2)\leftrightarrow(1,2)$	0.12636	0.1059	0.0914
$(2,1)\leftrightarrow(1,2)$	0.0242	0.0207	0.0158
$(2,2)\leftrightarrow(2,2)$	$<5\times10^{-4}$	$<5\times10^{-4}$	$<5\times10^{-4}$
$(1,3)\leftrightarrow(1,3)$	0.1453	0.1311	0.1171
	E_B (circular wire)		
Mode coupling	$N_\rho=3$	$N_\rho=4$	$N_\rho=5$
$[0,0]\leftrightarrow[0,0]$	0.01252	7.829×10^{-3}	5.334×10^{-3}
$[0,1]_s\leftrightarrow[0,1]_s$	0.0920	0.06626	0.04818
$[0,1]_a\leftrightarrow[0,1]_s$	~0	~0	~0
$[0,2]_s\leftrightarrow[0,2]_a$	0.08832	0.06873	0.05391
$[0,2]_s\leftrightarrow[0,2]_a$	8.41×10^{-3}	8.24×10^{-3}	6.469×10^{-3}
$[1,0]\leftrightarrow[1,0]$	2.152×10^{-3}	6.5685×10^{-3}	7.042×10^{-3}

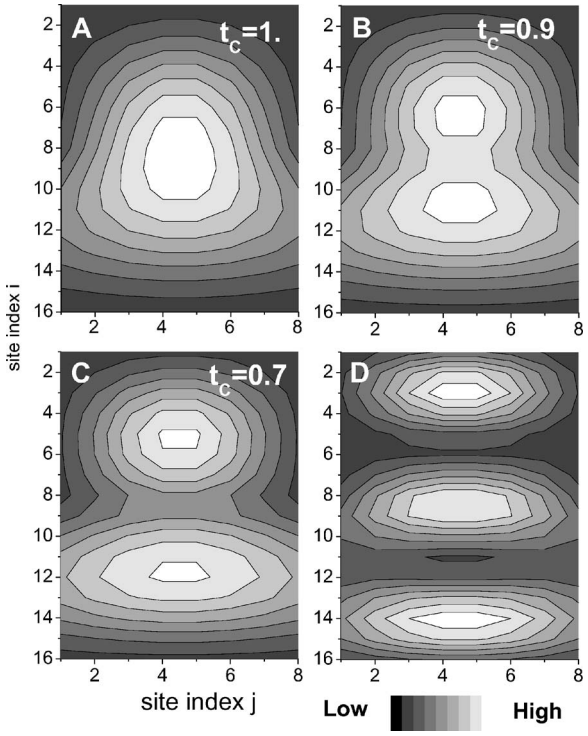

FIG. 12. (a), (b), and (c) The probability density of the bound state of $(1,1)\leftrightarrow(1,1)$ for various values of t_c. (d) The probability density of the quasibound state of $(1,2)\leftrightarrow(1,2)$.

sibound states give rise to prominent features around the second subband edge in the conductance. The probability density of the bound state of $(1,1)\leftrightarrow(1,1)$ is found from the LDOS by adding a small imaginary part to the energy $\mathrm{Im}[G(E+i\delta)]=-\delta|\phi_B|^2/[(E-E_B)^2+\delta^2]$ where ϕ_B denotes the bound state wave function. Putting $E=E_B$, we obtain the probability density using $\mathrm{Im}[G(E_B+i\delta)]=|\phi_B|^2/\delta$. Figures 12(a)–12(c) shows a cross section of the probability density for $t_c=0.7,0.9,1.0$. The position of the cross section is shown in Fig. 11 by the blue dash dot lines. In the strong coupling regime, $t_c=1$, the maximum probability density is at the interface between the two wires ($i=8$ and 9). When t_c is reduced, the peak of probability density splits into two peaks, the separation of which is very clear when $t_c=0.7$. The probability density of the quasibound state of $(1,2)\leftrightarrow(1,2)$ with $E_B=0.1059$ was found from LDOS in the scattering region and plotted in Fig. 12(d). It can be seen that strong interwire coupling produces a very large probability density at the interface between two wires. Without interwire coupling, there should be four peaks in the probability density, two in each wire. The interwire coupling merges the two peaks near the interface into one peak.

The direct use of LDOS for finding the probability density of the quasibound state $(2,1)\leftrightarrow(1,2)$ with $E_B=0.0207$ ($E=0.5673$) is not suitable, because the quasibound state $(2,1)\leftrightarrow(1,2)$ has a degenerate state $(1,2)\leftrightarrow(2,1)$. In LDOS, the probability densities of these two states are not separable. One approach to find the quasibound state probability density is using the approach described in Ando[36] to find the scattering state, which is, however, not convenient to use. We therefore use a symmetry projection operator $\hat{P}$ to isolate the $(2,1)\leftrightarrow(1,2)$ state, which is symmetrical with respect to the y-z plane and antisymmetrical with respect to the x-z plane, in the expression of Green's function. We define the modified Green's function G' by $G'=\hat{P}G\hat{P}=\Sigma_k\frac{\hat{P}\phi_k^*(i)\hat{P}\phi_k(j)}{E-E_k+i\delta}=\Sigma_{k'}\frac{\phi_{k'}^*(i)\phi_{k'}(j)}{E-E_{k'}+i\delta}$, where $\phi_{k'}$ denotes eigenstates that have the symmetry of $\hat{P}$, while ϕ_k denotes all the eigenstates. As a consequence, the LDOS of G' (i.e. $\mathrm{Im}[G'(i,i)]$) at energy $E=0.5673$ gives the probability density of the $(2,1)\leftrightarrow(1,2)$ state.

Figure 13 show the probability density of the quasibound state $(2,1)\leftrightarrow(1,2)$ on the two cross-sectional planes marked by blue dot-dash and red dot lines in Fig. 11 for an 8×8 square wire junction with $t_c=1$. In the upper wire, the prob-

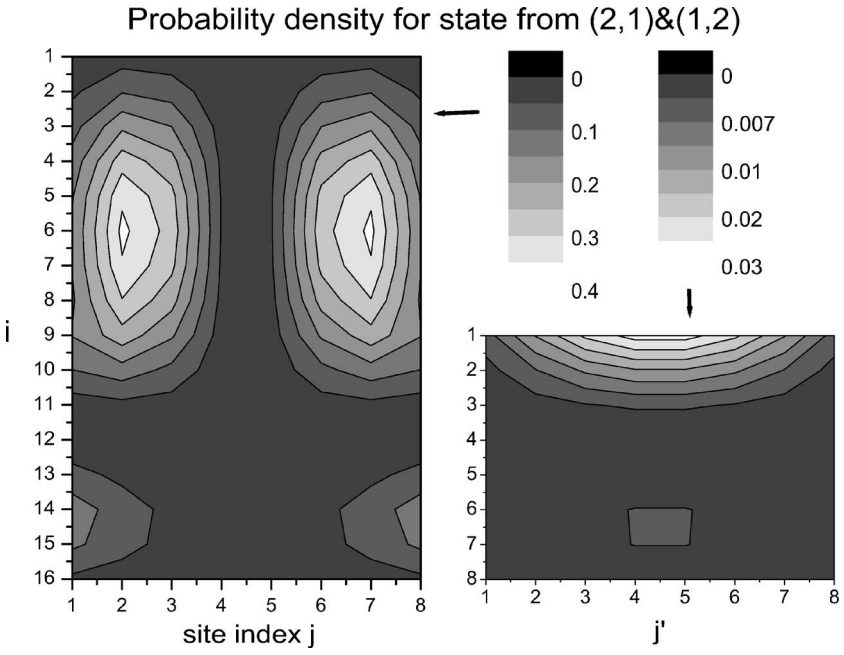

FIG. 13. The probability density of the quasibound state of $(2,1)\leftrightarrow(1,2)$ in the blue dot-dashed cross section (situated at index $j'=4$) and in the red dotted cross section (situated at index $j=4$) shown in Fig. 11.

ability density resembles that of mode (2,1), but with the peak density shifted towards the interface around $i=6$. In the lower wire (at site index $j=4$), the probability density is much smaller (note the difference in scales), because the cross-section for the lower wire is near to the middle of the junction and hence close to the node of the wave function. It is also interesting to note here that in the lower wire, the probability density has a symmetrical distribution and resembles mode (1,2). However, the peak of the probability density shifts to the interface between the two wires as a result of the interwire coupling.

IV. CONCLUSION

The quantum ballistic transport of electrons through a nanowire junction formed by putting one nanowire on top of another wire (the two wires are not lying in the same plane) was studied in detail using lattice tight-binding models and the Green's function approach. Nanowire junctions are basic building blocks of some nanowire devices, which were recently demonstrated experimentally. Results obtained in this study are useful for the development of these nanowire devices. Resonant dips and peaks were found in the interwire and intrawire conductances, which can be explained by the formation of bound and quasibound states at the cross-junction. A detailed analysis of how the conduction channels from different wires are coupled to form bound and quasibound states has been carried out for a simple 2×2 square model with the help of the projected Green's function. Although the model used in the analysis is relatively simple, the analysis clarifies the physics and provides a theoretical framework for analyzing the transport characteristics of other larger models in the present study (a 8×8 square wire model and a 8×11 and a 8×5 rectangular wire models). In general, quasibound states unbound in both wires give rise to resonant peaks in the interwire conductance as well as resonant dips in the intrawire conductance, while quasibound states unbound in only one wire give rise to only resonant dips in the intrawire conductance without any corresponding resonant peaks in the interwire conductance. However, there are exceptions in the latter case, when the quasibound state is coupled to other interwire scattering channels and a small peak can appear in G_{13}.

We have considered tight-binding models with large numbers of conduction channels (36, 64, and 100 channels) and find the optimum number of tight-binding site in the transverse plane for approximating the continuum model in a finite range of energy. For quantitative description of the conductance involving the lowest 6 subbands, we found that an 8×8 square model is sufficient. Tight-binding models with small numbers of conduction channels are also studied to find the minimum site number for qualitative description of the conductance (4×4 square is the minimal model found). The minimal model will be useful for studying the transport characteristics of nanowire networks formed from a large number of nanowires, where the adoption of a wire model with large conduction channel number is numerically infeasible. With proper energy scaling, the qualitative features of the conductances of $N\times N$ square wires with $N=4,6,8,10$ are similar and does not depend on N. This implies that the conductances of wires with different transverse dimensions have similar qualitative behavior. The effect of varying the interwire coupling strength is also investigated. Reduction of interwire coupling strength suppresses the interwire conductance at energy far from the subband edges. In the weak interwire coupling regime, larger interwire conductance is found at energy close to the subband edges. When only the first subband is occupied and the Fermi energy is far from the subband edge, the interwire conductance is close to zero in the weak coupling regime. We have compared the conductances of square and rectangular wires. Removal of subband degeneracy by changing the wire's cross section shifts the peaks and dips in the conductances and hence modifies the overall qualitative features. The dimension perpendicular to the junction (the z direction) has significant effect on the overall magnitude of the interwire conductance. Decrease of the z direction dimension increases the interwire conductance and decreases the intrawire conductance, indicating that junctions formed from ribbon-like wires have lower resistances. Degeneracy of subbands due to the higher symmetry of a square cross section are found to increase the interwire conductance. The conductances of circular wire junctions are qualitatively very similar to those of square wire junctions except for the energy positions of the features. Some conductance dip which can be found in square wire junctions disappears in circular wire junction, because the weaker interwire coupling in circular wire junctions makes the dip difficult to be resolved. The transverse dimension was found to have significant effect on the bound and quasibound state energies, which are generally increased by decreased in the transverse dimension. In bound and quasibound states formed at the junction, high electron density can be found at the interface between two wires when interwire coupling is strong.

ACKNOWLEDGMENT

The work described in this paper was fully supported by a grant from the Research Grants Council of the Hong Kong Special Administrative Region, China [Project No. CityU 100303].

APPENDIX A: DEFINITION AND PROPERTIES OF THE PROJECTED GREEN'S FUNCTION

For the discussion of the definition and general properties of projected Green's function, we consider the example of a quasibound state formed by mixing one bound state of a higher subband with a continuum of unbound states of a lower subband. The discussion can readily be extended to the case of many bound states and continua. Denoting the bound state wave function by $|\phi\rangle$ and the unbound state wave function by $|\chi_E\rangle$. The continuum of eigenstates formed from the mixing of $|\phi\rangle$ and $|\chi_E\rangle$ is given by $|\psi(E)\rangle=a(E)|\phi\rangle+\int b_{E'}(E)|\chi_{E'}\rangle dE'=a(E)|\phi\rangle+|\vartheta(E)\rangle$ according to Fano.[37] Since $|\vartheta(E)\rangle$ is a linear combination of lower subband eigenstates and $|\phi\rangle$ is a linear combination of higher subband eigenstates, $|\vartheta(E)\rangle$ is orthogonal to $|\phi\rangle$ and $\langle\phi|\vartheta(E)\rangle=0$.

Substituting the expression of $|\psi(E)\rangle$ into the definition of Green's function $G(E)$, we obtain $G(E)=\frac{|\phi\rangle\langle\phi|}{E-E_B+i\Gamma}+g_B(E)$, where

$$g_B(E)=\int \frac{dE'}{E-E'+i\delta}(a(E')|\phi\rangle\langle\vartheta(E')|+a^*(E')|\vartheta(E')\rangle\langle\phi| + |\vartheta(E')\rangle\langle\vartheta(E')|).$$

A detailed derivation of this expression is given in Appendix B. It is worth pointing out here this expression is obtained with the assumption that Γ is very small in comparison with the range of integration of E. Consider a wave function $|\eta\rangle$, which is a linear combination of eigenstates of the higher subband and is a state vector in the subspace spanned by the eigenstates of the higher subbands. If $|\eta\rangle$ is not orthogonal to $|\phi\rangle$, i.e., $\langle\phi|\eta\rangle\neq 0$. The diagonal maxtrix element of the Green's function $\langle\eta|G|\eta\rangle=\frac{|\langle\eta|\phi\rangle|^2}{E-E_B+i\Gamma}$ has a Lorentzian peak in the imaginary part spectrum, because $\langle\eta|g_B(E)|\eta\rangle=0$. Since $|\eta\rangle$ must be confined within the subspace of higher subband eigenstates, constructing this matrix element resembles projecting the Green's function onto the subspace, and this is the reason why we refer to this matrix element as the projected Green's function. The simplest way to make sure that $\langle\phi|\eta\rangle\neq 0$ is to choose $|\eta\rangle=W_{[i]}\delta_{j,k}$, where $|W_{[i]}\rangle$ is the transverse mode eigenfunction of the subband i and $\delta_{j,k}$ is the Kronecker δ denoting that the wave function $|\eta\rangle$ is localized in the lattice plane $j=k$ (k should not be at a node of the wave function). If $|\phi\rangle=\Sigma_{i'}c_{i'}|W_{[i']}\rangle|U_{[i']}\rangle$, where $U_{i'}$ is the longitudinal part of the wave function. We have $\langle\eta|G|\eta\rangle=\frac{|c_i|U_{[i],j=k}\rangle|^2}{E-E_B+i\Gamma}$. If a Lorentzian peak is found in the imaginary part of the diagonal projected Green's function $\langle\eta|G|\eta\rangle$, the subband i is a component of the bound state $|\phi\rangle$ and quasibound state $|\psi\rangle$. To find out whether the unbound states of a lower subband is a component of the $|\psi\rangle$, one can examine the projected Green's function element, $\langle\eta|G|\mu\rangle$, where $|\mu\rangle$ is a linear combination of the unbound eigenstates of the lower subband and $\langle\mu|\vartheta\rangle\neq 0$. As for $|\eta\rangle$, one can choose $|\mu\rangle=W_{[r]}\delta_{j,k}$, where r is the index of the lower subband. Since our aim is to find out how the subbands from different wires are mixed together to obtain the bound state and quasibound state, it is necessary to plot two projected Green's function, one for the upper wire and one for the lower wire. To simplify the analysis, it is possible to plot only one projected Green's function $\langle\eta_U|G|\eta_L\rangle$, where $|\eta_U\rangle$ and $|\eta_L\rangle$ are states localized respectively in the upper and lower wires. However, the imaginary part of this mixed projected Green's function $\langle\eta_U|G|\eta_L\rangle=\frac{\langle\eta_U|\phi\rangle\langle\phi|\eta_L\rangle}{E-E_B+i\Gamma}$ does not have a Lorentzian peak if $\langle\eta_U|\phi\rangle\langle\phi|\eta_L\rangle=c+id$ is not real. The imaginary part of this mixed projected Green's function is $\frac{c\Gamma}{(E-E_B)^2+\Gamma^2}+\frac{d(E-E_B)}{(E-E_B)^2+\Gamma^2}$, which mixes the real and imaginary parts of the line shape function $1/(E-E_B+i\Gamma)$. If Γ is small when the quasibound state has long lifetime, one can see rapidly changing features in the mixed projected Green's function indicating that these subbands are important components of the quasibound state. On the other hand, one can combine two projected Green's functions as in $(\langle\eta_U|G|\eta_L\rangle+\langle\eta_L|G|\eta_U\rangle)/2=c/(E-E_B+i\Gamma)$ so that the quasibound state always give rise to a Lorentzian peak in the imaginary part. Nevertheless, in the present study, we found that $\langle\eta_L|G|\eta_U\rangle$ displays some rapidly changing features around the energy E_B due to the presence of the factor $1/(E-E_B+i\Gamma)$, when the subbands η_L and η_U are important components of the quasibound states. These rapidly changing features are already useful indicators for confirming the contribution of η_L and η_U to the quasibound state and, thus, it is not necessary to consider the more properly defined expression $(\langle\eta_U|G|\eta_L\rangle+\langle\eta_L|G|\eta_U\rangle)/2$. In reality Γ may not be very small and hence the prominent features in the projected Green's function may not be exactly described by the line shape function $1/(E-E_B+i\Gamma)$.

APPENDIX B: DERIVATION OF EXPRESSION FOR GREEN'S FUNCTION IN APPENDIX A

The Green's function is given by

$$G(E)=\int dE'\frac{|\psi(E')\rangle\langle\psi(E')|}{E-E'+i\delta}=\int\frac{dE'}{E-E'+i\delta}|a(E)|^2|\phi\rangle\langle\phi| + \int\frac{dE'}{E-E'+i\delta}(a(E')|\phi\rangle\langle\vartheta(E')|+a^*(E')|\vartheta(E')\rangle\langle\phi| + |\vartheta(E')\rangle\langle\vartheta(E')|)=\int\frac{dE'}{E-E'+i\delta}|a(E)|^2|\phi\rangle\langle\phi| + g_B(E),$$

where

$$g_B(E)=\int \frac{dE'}{E-E'+i\delta}(a(E')|\phi\rangle\langle\vartheta(E')|+a^*(E')|\vartheta(E')\rangle\langle\phi| + |\vartheta(E')\rangle\langle\vartheta(E')|).$$

According to Fano,[37] $|a(E)|^2=\frac{\Gamma/\pi}{(E-E_\phi+\Delta(E))^2+\Gamma^2}$. Considering the case of a sharp resonance (assuming Γ is small in comparison with the integration range of E) and $\Delta(E)$ does not depend strongly on E within the resonance. $|a(E)|^2\cong\frac{\Gamma/\pi}{(E-E_B)^2+\Gamma^2}$ and $\int dE'\frac{|a(E')|^2}{E-E'+i\delta}\cong\frac{1}{E-E_B+i\Gamma}$.

As a result, $G(E)=\frac{|\phi\rangle\langle\phi|}{E-E_B+i\Gamma}+g_B(E)$.

*Corresponding author. On sabbatical leave at Nanoscience & Nanotechnology Cluster, Nanyang Technological University, Singapore. Email address: apkschan@cityu.edu.hk

[1] S. Saito, Science **278**, 77 (1997); P. L. McEuen, Nature (London) **393**, 15 (1998).
[2] C. Dekker, Phys. Today **52**, 22 (May 1999).
[3] M. S. Dresselhaus, G. Dresselhaus, and P. C. Eklund, *Science of Fullerenes and Carbon Nanotubes* (Academic Press, San Diego, 1996).
[4] X. Daun, Y. Huang, Y. Cui, J. Wang, and C. M. Leiber, Nature (London) **409**, 66 (2001).
[5] M. S. Gudiksen, L. J. Lauhon, J. Wang, D. C. Smith, and C. M. Leiber, Nature (London) **415**, 617 (2002).
[6] D. Whang, S. Jin, Y Wu, and C. M. Leiber, Nano Lett. **3**, 1255 (2003).
[7] Y. Huang, X. Duan, Y. Cui, L. J. Lauhon, K-H. Kim, and C. M. Lieber, Science **294**, 1313 (2001);
[8] Y. Huang, X. Duan, Q. Wei, and C. M. Lieber, Science **291**, 630 (2001).
[9] A. DeHon, P. Lincoln, and J. E. Savage, IEEE Trans. Nanotechnol. **2**, 165 (2003).
[10] A. DeHon, IEEE Trans. Nanotechnol. **2**, 23 (2003).
[11] G. Snider, P. Kuekes, and R. S. Williams, Nanotechnology **15**, 881 (2004).
[12] X. Duan, J Wang, and C. M. Lieber, Appl. Phys. Lett. **76**, 1116 (2000).
[13] W. S. Shi, Y. F. Zheng, N. Wang, C. S. Lee, and S. T. Lee, Appl. Phys. Lett. **78**, 3304 (2001).
[14] N. Wang, Y. F. Zhang, Y. H. Tang, C. S. Lee, and S. T. Lee, Appl. Phys. Lett. **73**, 3902 (1998).
[15] C. C. Tang, S. S. Fan, H. Y. Dang, P. Li, and Y. M. Liu, Appl. Phys. Lett. **77**, 1961 (2000).
[16] Y. Cui, X. Duan, J. Hu, and C. M. Lieber, J. Phys. Chem. B **104**, 5213 (2000)
[17] X. Duan, Y. Huang, R. Agarwal, C. M. Lieber, Nature (London) **421**, 241 (2003).
[18] X. Duan, C. Wu, V. Saki, J. Chen, J. W. Parce, S. Empedocles, and J. L. Goldman, Nature (London) **425**, 274 (2003)
[19] Y. Huang X. Duan, Y. Cui, and C. M. Lieber, Nano Lett. **2**, 101 (2002).
[20] M. Buttiker, Phys. Rev. Lett. **57**, 1761 (1986).
[21] D. G. Ravenhall, H. W. Wyld, and R. L. Schult, Phys. Rev. Lett. **62**, 1780 (1989).
[22] Y. Takagaki and K. Ploog, Phys. Rev. B **48**, 11508, (1993).
[23] Y. Takagaki and K. Ploog, Phys. Rev. B **49**, 1782 (1994).
[24] Yu. B. Gaididei *et al.*, J. Phys.: Condens. Matter **4**, 7103 (1992).
[25] J. H. Wei and K. S. Chan, Phys. Lett. A **341**, 224 (2005).
[26] D. K. Ferry and S. M. Goodrich, *Transport in Nanostructures* (Cambridge University Press, Cambridge UK 1997).
[27] T. Itoh, Phys. Rev. B **52**, 1508 (1995).
[28] H. Q. Xu, Phys. Rev. B **66**, 165305 (2002).
[29] P. A. Orellana, M. L. Ladron de Guevara, M. Pacheco, and A. Latge, Phys. Rev. B **68**, 195321 (2003)
[30] P. A. Orellana and M. Pacheco, Phys. Rev. B **71**, 235330 (2005).
[31] P. A. Orellana F. Dominguez-Adame, I. Gomez, and M. L. Landron de Guevara, Phys. Rev. B **67**, 085321 (2003).
[32] S. Datta, *Electronic Transport in Mesoscopic Systems* (Cambridge University Press, Cambridge, U.K., 1995).
[33] S. Rotter, J. Z. Tang, L. Wirtz, J. Trost, and J. Burgdörfer, Phys. Rev. B **62**, 1950 (2000).
[34] Z. Shao, W. Porod, and C. S. Lent, Phys. Rev. B **49**, 7453 (1994).
[35] W. Porod, Z. Shao, and C. S. Lent, Appl. Phys. Lett. **61**, 1350 (1992).
[36] T. Ando, Phys. Rev. B **44**, 8017 (1991).
[37] U. Fano, Phys. Rev. **124**, 1866 (1961).